Large and Optimized Thermal Chiral Anomaly in Weyl Semimetal Bi-Sb

Joon Sang Kang,[1,2,*,†] Dung Vu[1,†] Minyue Zhu,[1] and Joseph P. Heremans[1,3,4]

[1]*Department of Mechanical and Aerospace Engineering, The Ohio State University, Columbus, Ohio 43210, USA*

[2]*Department of Mechanical Engineering, Korea Advance Institute of Science and Technology, Daejeon, 34141, South Korea*

[3]*Department of Physics, The Ohio State University, Columbus, Ohio 43210, USA*

[4]*Department of Materials Science and Engineering, The Ohio State University, Columbus, Ohio 43210, USA*

Weyl semimetals are bulk solids in which chiral anomalies, i.e., negative magnetoelectric and magnetothermal resistances, exist as a result of the chiral properties of the Weyl fermions. The thermal chiral anomaly has potential in devices that actively control heat fluxes; these would be an early application of topological properties, realized after the materials are optimized. Here, we optimized the band structure of $Bi_{1-x}Sb_x$ alloys in the topological insulator phase and in their field-induced Weyl semimetal phases to maximize the thermal chiral anomaly by changing the Sb concentration and by doping $Bi_{1-x}Sb_x$ alloys either with n-type Te or with p-type Sn. We show that the chiral anomalies are maximized when the chemical potential is at the Weyl points and that Weyl fermions are protected against scattering on phonons and neutral defects but not necessarily on charged particles like ionized impurities and electrons in trivial pockets. In our optimum material, around 30% of the total heat (carried by phonons, trivial electrons, and the chiral anomaly) is carried by the anomalous heat current (the chiral anomaly). The latter is highly switchable under a magnetic field. The maximum effect we observe is an anomalous thermal conductivity at 7 T that is 700% larger than the zero-field electronic thermal conductivity at $T = 40$ K in a $x = 0.1$ sample with p-type doping to 3.90×10^{15} cm^{-3} with a mobility of $2\,350\,000$ cm^2 V^{-1} s^{-1}.

I. INTRODUCTION

Over more than a decade, theoretical predictions [1] and experimental realizations [2] of topological order in crystals have been of great interest in condensed-matter physics. It predicts exotic quantum transport behavior and has potential applications in high-performance devices. Topological insulators (TIs) were studied first; ideally, they have a bulk band gap, but gapless surface states exist with a Dirac dispersion, in which charge-carrier transport is protected by time-reversal or mirror symmetry [3]. However, the presence of bulk conduction in most real material systems provides a strong scattering channel for surface electrons [4]. This limits potential applications of these materials in transport devices. Weyl semimetals, where the bulk-electron properties are dominated by topological effects, do not suffer from these limitations. Like TIs, the Weyl semimetal (WSM) phase is also induced from strong spin-orbit coupling [5]. In k space, the dispersion of conduction and valence bands (CBs and VBs, respectively) in WSMs is linear and intersects at special points, the Weyl

points (WPs), which are the source and sink of Berry curvature. When the chemical potential is at the Weyl-point energy and there are no trivial bands at the same energy [6], the materials are ideal Weyl semimetals. This situation can be achieved in the $Bi_{1-x}Sb_x$ system for optimal x values determined in this work. In ideal WSMs, the net charge is neutral, the dispersion of fermions is linear, and they are massless and move like photons with only a group velocity and a Berry curvature in their equations of motion. However, unlike TIs, WSMs possess unique bulk transport properties, particularly chiral and gravitational anomalies [7].

The anomalies exist at any value of field, but we concentrate on the situation where the magnetic field, B, is high enough that the charge carriers are at the last Landau level, the extreme quantum limit (EQL). In spite of mobilities in the order of a 10^6 cm^2 V^{-1} s^{-1}, the magnetoresistance recorded at 2 K for our samples shows no Shubnikov-de Haas oscillations, indicating that the samples are in the EQL. In the EQL [see Fig. 1(a)], the last Landau level has only one velocity on one Weyl point (called right movers, W_R) and the opposite velocity on the other (called left movers, W_L) due to chiral motion of the fermions [8]. The chiral anomaly [8] arises when both electrical and

---

*jskang1@kaist.ac.kr

†J. S. Kang and D. Vu. contributed equally to this work.

magnetic fields are applied parallel to Weyl nodes separation ($E||B$). In the EQL, WSM bulk-electron transport is topologically protected from back scattering like surface electrons in TIs. Backscattering is only possible accompanied by a chirality flip of Weyl fermions. The electric field creates an imbalance between the fermion concentration at W_R and W_L, proportional to E and B, as shown in Fig. 1(a). This charge-carrier imbalance is an anomalous electrical current. It is measured as an anomalous negative magnetoresistance (NMR), which is expressed as [9]

$$\sigma_a = N_w \frac{e^3 v \tau}{4\pi^2 \hbar^2} B, \qquad (1)$$

where N_w, e, v, τ, $\hbar$, and B are the number of degenerate Weyl node pairs, electron charge, electron velocity, inter-Weyl-point relaxation time, Planck's constant, and magnetic field, respectively.

Often called the gravitational anomaly because it is based on the same equations as those used in cosmology, the thermal chiral anomaly exists in WSMs when a thermal gradient is applied parallel to the magnetic field ($\nabla T || B$) along the direction of the Weyl-point separation. In ideal Weyl semimetals, no carrier- or charge-density imbalance results from the application of $\nabla T || B$, but an energy imbalance between left movers and right movers arises that is proportional to T and B. Figure 1(b) shows a schematic of the thermal chiral anomaly. This energy imbalance creates a measurable anomalous electronic thermal conductivity, which is expressed by [10]

$$\kappa_a = N_w T \frac{\pi^2}{3} \frac{k_B^2 e v \tau}{4\pi^2 \hbar^2} B, \qquad (2)$$

where T and k_B are the temperature and Boltzmann constant, respectively.

Over the last decade, much research has reported NMR in WSM candidates, such as NbP, TaAs, and WTe$_2$, as the smoking gun of chiral anomalies [7,11,12]. However, these data show varying intensities of the chiral anomaly across different materials and samples, which is inconsistent with the concept that anomalous currents are topologically protected. Based on theory, at least, the anomalous currents in a given material should be reproducible. To date, there are no systematic experimental studies about how and why the intensity of a chiral anomaly (NMR ratio) varies from sample to sample, or by how much it is affected by the presence of trivial bands in the Fermi surface, and why it highly depends on temperature. Additionally, due to the Dirac-like dispersion near WPs, WSMs have very high mobilities up to several millions of cm^2 V^{-1} s^{-1} at low temperature. Consequently, the NMR of WSMs is extremely vulnerable to extrinsic effects (i.e., effects where the charge-current distribution across the physical sample is perturbed by the magnetic field, so that the effects measured are not due to the physics in the material but to the sample and electrode geometry). The extrinsic signals can arise in three different ways and need to be carefully addressed in sample preparation, dimensions, and alignment to ensure accurate magnetoresistance measurements [9].

The first source of extrinsic signals is current jetting [13,14], which gives rise to a negative longitudinal MR, similar to the chiral anomaly. The second extrinsic effect is the galvanomagnetomorphic effect [15–17], which can also generate a negative longitudinal MR. The third and most important effect is the geometrical MR [18], an extrinsic signal that leads to a positive MR. This effect arises when the sample surface is not smooth, when the sample width is not much smaller that the sample length, or when there is a slight misalignment between the magnetic field and the current flow lines during sample mounting.

Magnetothermal conductivity measurements do not require these heroic efforts, since no electrical current is flowing, and the lattice thermal conductivity spontaneously homogenizes the heat-flux distribution inside the sample and thermal-energy redistribution between Weyl fermions and phonons helps to even out extrinsic effects. Not only a point of fundamental physics interest, the thermal chiral anomaly also holds promise for practical device applications.

Because the thermal chiral anomaly is proportional to the magnetic field, the thermal conductivity of a solid can be controllable by applying a magnetic field, provided the phonon contribution can be minimized, as is the case in most solids below 1 K. We point out that the mechanism offers results in a thermal conductivity that is higher at high field than at low field. Therefore, the present mechanism and the classical mechanism based on a positive magnetoresistance and the Wiedemann-Franz law [such as that seen in Bi$_{1-x}$Sb$_x$ alloys when the magnetic field is oriented perpendicularly to the (001) axis [9]] form a complementary pair of switches, where one is open when the other is closed. All-solid-state thermodynamic heat engines (generators, refrigerators) without mechanical moving parts can be constructed by using a complementary pair of solid-state thermal switches in conjunction with an electrocaloric or magnetocaloric material. Switching, rectifying, and regulating heat flow by using thermal switches can also potentially boost thermodynamic efficiency of cycles [19].

Here, we work with the Bi$_{1-x}$Sb$_x$ alloy system of narrow-gap semiconductors and topological insulators. We observe a very large thermal chiral anomaly in Bi$_{1-x}$Sb$_x$ and, more significantly, we explain how the band structure of Weyl semimetals can be engineered to maximize the thermal (and electrical) chiral anomaly in them. Our discovery is applicable not only to the Bi$_{1-x}$Sb$_x$ system, but also to other Weyl semimetals, such as Na$_3$Bi, TaAs, and GdPtBi.
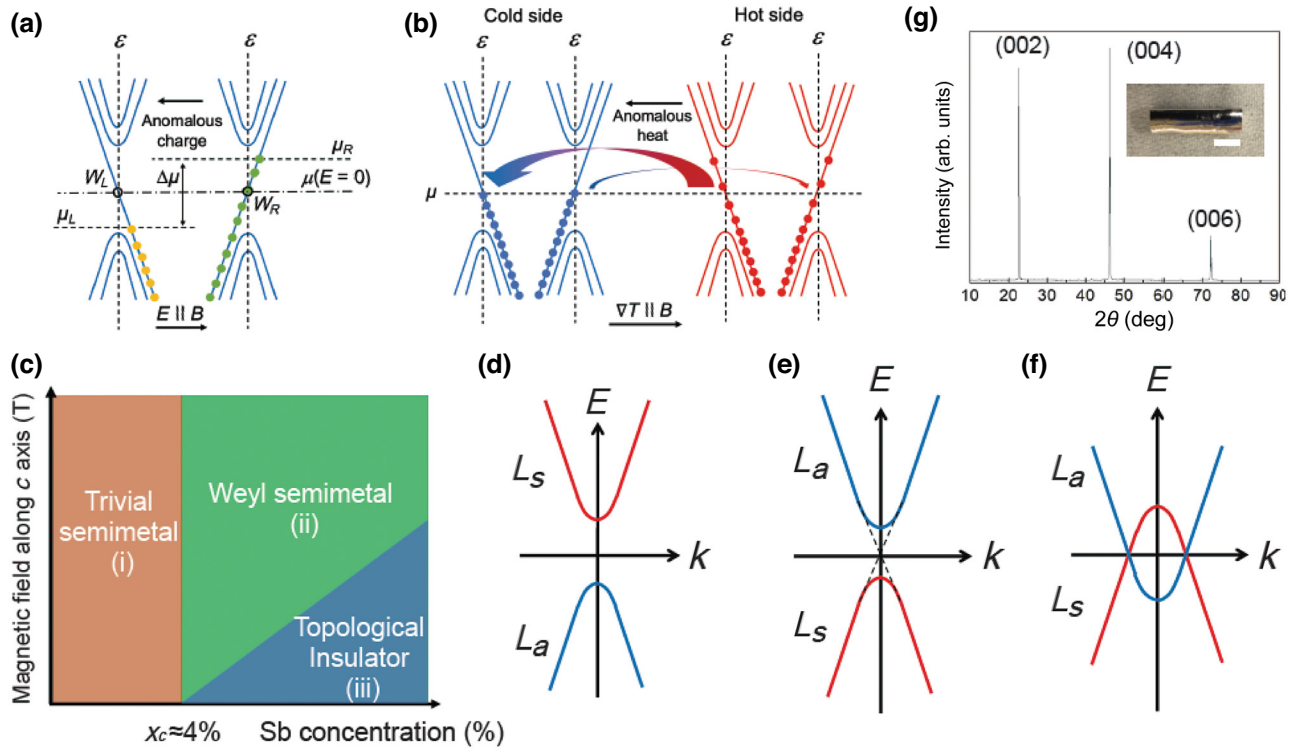
FIG. 1.   Schematic of chiral anomaly and sample characterization. (a) Schematic of electrical chiral anomaly: electric field induces a shift in chemical potential between Weyl points that results in charge-carrier imbalance between the Weyl points, which generates an anomalous charge current and conductivity. (b) Schematic of thermal chiral anomaly: thermal gradient induces no change in chemical potential or charge-carrier density, but an imbalance between the charge-carrier energy at both Weyl points. This gives an imbalance in heat carried by the Weyl fermions between the hot and cold sides of the sample (curved arrows), and thus, an anomalous heat current and thermal conductivity. (c) Topological phase diagram of $Bi_{1-x}Sb_x$ solid solutions through the electronic band structure of L-point carriers, (d) in the trivial semimetal phase (i), (e) in the topological insulator phase (ii), and (f) in the field-induced Weyl semimetal phase (iii). (g) X-ray diffraction data of the $Bi_{0.95}Sb_{0.05}$ alloy; inset shows an as-grown $Bi_{0.95}Sb_{0.05}$ crystal with a scale bar of 1 cm.

$Bi_{1-x}Sb_x$ alloys form a full solid solution for $0 < x < 1$ and maintain the crystal structure of Bi (trigonal with the R-$3m$ space group). Because Bi and Sb are both group V elements and have the same number of valence electrons, the stoichiometric ratio, x, between Bi and Sb does not affect the electron or hole concentrations, and the chemical potential is therefore only determined by residual impurities of the starting material (Bi and Sb), intentional doping, and the temperature. This situation is akin to that of elemental semiconductors and their isoelectronic alloys, such as Si and $Si_{1-x}Ge_x$: minimizing unintentional doping requires only starting-material purification, not exquisite stoichiometry control. $Bi_{1-x}Sb_x$ is the only WSM system so far that enjoys this critical advantage and allows us to optimize the material parameters reliably and controllably.

Figure 1(c) shows the topological phase diagram of $Bi_{1-x}Sb_x$, which has three different electronic band phases up to $x = 0.25$. Based on band-structure calculations reported in Sec. II of the Supplemental Material to Ref. [9], in the absence of any magnetic field, $Bi_{1-x}Sb_x$ undergoes four electronic phase changes with varying x [20]: (i) at $x < 0.04$, $Bi_{1-x}Sb_x$ is a trivial semimetal with overlapping electron bands at the L point of the Brillouin zone and hole bands at the T points. There is a direct band gap located at L points, where there is a CB labeled L_s and a VB labeled L_a [Fig. 1(d)]. (ii) At $0.04 < x < 0.09$, the L_s and L_a bands are inverted [Fig. 1(e)], but the trivial T-hole band still lies across the L bands, leading to an indirect gap between L_a and T-hole bands; (iii) at $0.09 < x < 0.15$, the T-hole band moves below the L_a band, making $Bi_{1-x}Sb_x$ a direct-band-gap TI, and (iv) at $0.15 < x < 0.224$, another trivial hole band at the H point of the Brillouin zone moves above the L-point valence band, resulting in an indirect band gap again between L_s and H-hole bands. Applying a magnetic field along the trigonal (001) direction of the $Bi_{1-x}Sb_x$ alloys separates the bands into Landau levels. Also, based on band-structure calculations in Ref. [9], in a trigonal magnetic field, because of the large negative g factor ($g = -71$) along (001) and Zeeman splitting [9], the last Landau levels of the CB and VB can be shifted toward each other and form WPs [Fig. 1(f)]. $Bi_{1-x}Sb_x$ ($0.04 < x < 0.25$) is thus a magnetic-field-induced type-I Weyl semimetal.

TABLE I. Summary of sample properties used in this study.

Sample No.	Lattice constant (Trigonal axis)	Sb concentration (%)	Mobility at 10 K ($cm^2\,V^{-1}\,s^{-1}$)	Carrier concentration at 10 K (cm^{-3})
Control	11.8635 ± 0.0025	0		
A1	11.8534 ± 0.0037	2.1 ± 0.7	1.75×10^6	8.92×10^{16}
A2	11.8453 ± 0.0038	3.3 ± 0.7	1.94×10^6	8.32×10^{16}
A3	11.8415 ± 0.0032	4.1 ± 0.6	3.47×10^6	5.67×10^{16}
A4	11.8353 ± 0.0041	5.3 ± 0.8	1.34×10^6	1.41×10^{16}
A5	11.8256 ± 0.0032	7.2 ± 0.6	3.97×10^5	3.20×10^{15}
A6	11.8088 ± 0.0034	10.5 ± 0.7	2.14×10^6	3.78×10^{15}
A7	11.7954 ± 0.0038	13.2 ± 0.7	2.24×10^6	4.16×10^{15}
A8	11.7693 ± 0.0042	18.4 ± 0.8	$2.20 \text{ v } 10^4$	2.19×10^{15}
A9	11.7572 ± 0.0048	20.3 ± 0.9	7.85×10^5	6.00×10^{14}
A10	11.7474 ± 0.0051	22.4 ± 1	9.13×10^5	3.10×10^{15}
S1	11.8123 ± 0.0044	9.8 ± 0.8	8.72×10^5	9.42×10^{16} (n)
S2	11.8080 ± 0.0047	10.6 ± 0.9	8.91×10^5	2.62×10^{17} (n)
S3	11.8108 ± 0.0048	10.1 ± 0.9	1.37×10^5	8.01×10^{17} (n)
S4	11.8094 ± 0.0044	10.4 ± 0.8	1.09×10^6	5.57×10^{16} (p)
S5	11.8066 ± 0.0046	10.9 ± 0.9	2.35×10^6	3.90×10^{15} (p)
S6	11.8108 ± 0.0050	10.1 ± 1	1.08×10^6	3.62×10^{16} (p)
S7	11.8123 ± 0.0051	9.8 ± 1	4.18×10^3	9.05×10^{18} (p)

The WPs of $Bi_{1-x}Sb_x$ ($0.04 < x < 0.25$) are located near the L point in the Brillouin zone, and these are separated mostly along (001) in real space. The field, B, required to form a WSM, in principle, depends linearly on x because the bulk band gap of $Bi_{1-x}Sb_x$ scales linearly with x and the Zeeman energy and the orbital Landau-level separations are linear in B.

To maximize the thermal chiral anomaly in their Weyl phase, we optimized the band structure and Fermi level of the $Bi_{1-x}Sb_x$ alloys. First, we experimented with different $Bi_{1-x}Sb_x$ alloys by changing the Sb composition, x, from 0 to 0.224 and uncovered the effect of band morphology on the amplitude of the thermal chiral anomaly. Next, we doped the samples, but retained a composition where the thermal chiral anomaly was maximum, either with n-type Te or with p-type Sn. In the end, the maximum effect we observe is an anomalous thermal conductivity at 7 T that is 700% larger than the electronic thermal conductivity at $T = 40$ K in a $x = 0.105$ sample with p-type doping to 3.90×10^{15} cm^{-3} and a mobility of 2 350 000 cm^2 V^{-1} s^{-1} at 10 K. From this study, we conclude that the maximum thermal chiral anomaly is achieved in samples with a zero-field TI state that is a direct-gap semiconductor with no trivial bands in the energy landscape. The optimum doping level is such that the chemical potential falls as close as possible to the Weyl points. We report that the chiral anomaly is strongly influenced by the presence of trivial electron and hole bands. Also, the temperature-dependent doping studies result in the conclusion that ionized impurities scatter Weyl fermions. We also briefly mention the possible effect of the temperature dependence of the band structure on the thermal chiral anomaly.

II. RESULTS AND DISCUSSION

High-quality Bi-Sb crystals are synthesized by the traveling-molten-zone method [21] with a seed crystal, which is carefully chosen according to the binary phase diagram of $Bi_{1-x}Sb_x$. The inset of Fig. 1(g) shows an as-grown $Bi_{0.96}Sb_{0.04}$ single crystal. We synthesized 18 samples, as summarized in Table I. Eleven undoped samples with stoichiometric ratios of $x = 0$ to $x = 0.224$ are labeled A1–A10, with an additional control sample. Seven doped $Bi_{0.9}Sb_{0.1}$ samples are labeled S1–S7. The stoichiometric ratio between Bi and Sb is determined by measuring lattice constant using the x-ray diffraction (XRD) method [22]. Figure 1(g) shows the XRD peaks of the $Bi_{0.96}Sb_{0.04}$ sample. Clearly, only (001) crystallographic direction peaks are detected with small full width at half maximum peaks, which indicate single crystallinity and the high quality of our sample. The lattice constant of Bi-Sb alloys decreases when x is increased, as shown in Table I, following Vegard's law [22].

The quality of undoped $Bi_{1-x}Sb_x$ samples is further characterized by the Hall effect and mobility measurements. To avoid chiral-anomaly-induced misinterpretation of Hall measurements, the magnetic field, B, is applied along the (010) direction and the Hall voltage is measured along the (100) direction with the current along the (001) direction. Because $Bi_{1-x}Sb_x$ is an intrinsic semiconductor, a two-carrier system, we use a small magnetic field (<0.05 T) to extract the major carrier concentration and mobility (see the Method section in the Supplemental Material [24]). Figure 2(a) shows the mobility of undoped samples from $x = 0.021$ to $x = 0.224$. Mobilities of most samples are near 1 000 000 cm^2 V^{-1} s^{-1} at

10 K and over 10 000 cm^2 V^{-1} s^{-1} at room temperature, which indicates identically excellent sample quality. At $x = 0.04$, we observe a mobility of 3 000 000 cm^2 V^{-1} s^{-1} at 10 K, which is highest among the compositions, presumably due to the Dirac dispersion of the L-point carriers in zero field when $x = 0.04$[10]. Figure 2(b) shows the temperature-dependent carrier concentration of Bi$_{1-x}$Sb$_x$ samples. The carrier concentration of all samples increases with temperature due to thermal excitation. At $x < 0.05$, the carrier concentration saturates to a value in the 10^{17} cm^{-3} range for $T < 30$ K; this behavior is consistent with the semimetallic nature of the band structure. In contrast, at $x > 0.05$, carrier concentrations keep decreasing as the temperature is decreased to 10 K; this is attributed to the intrinsic semiconducting nature of TIs. Remarkably, the carrier concentration of the $x = 0.203$ sample freezes out to 6.5×10^{14} cm^{-3} at 10 K, suggesting an exceptionally low residual dopant concentration. Bismuth has 6×10^{22} atoms per cm^3 and this residual concentration indicates the presence of about one unintentional dopant atom among 10^8 atoms of Bi, attesting to the extremely high quality of the sample. The temperature dependence of the zero-field thermal conductivity of the 10.5% and 13.2% samples are very similar to those reported in Ref. [9] for 12% and 15% samples; they are analyzed in terms of lattice and electronic contributions there.

Next, we measured the magnetothermal conductivity of ten undoped samples with both ∇T and B in the (001) direction. We first describe the magnetothermal conductivity of semimetal samples with $x < 0.04$. At 75 K, the thermal conductivity of Bi$_{0.98}$Sb$_{0.02}$ decreases quickly from 7.4 to 6.6 W m^{-1} K^{-1} when the magnetic field increases from 0 to 1 T, then plateaus at a higher B. The decrease comes from the ordinary magnetoresistance in this intrinsic semiconductor [$\sigma/\sigma_0 \sim 1/(1 + (\mu B)^2)$], and saturation is reached when the phonon thermal conductivity dominates. We do not observe any anomalous magnetothermal conductivity behavior in the Bi$_{0.98}$Sb$_{0.02}$ sample and the magnetothermal conductivity shows behavior similar to that of the trivial semimetal Bi (see Fig. S2 within the Supplemental Material [24]). Samples with $x > 0.04$ [see Fig. S1(b) within the Supplemental Material [24]] show anomalous magnetothermal conductivity behavior due to the thermal chiral anomaly. Below 1 T, it behaves like a semimetal or an intrinsic narrow-gap semiconductor because the magnetic field is not sufficient to induce the phase change from a TI to a Weyl semimetal at the L point. However, when $B > 3$ T, samples with $x > 0.04$ show a significant thermal conductivity increase, which comes from the thermal chiral anomaly. We observe this phenomenon at temperatures up to 200 K. Since the Debye temperature of the alloys is in the order of 100 K [23], this indicates that the Weyl fermions are little affected by phonon scattering. We showed in Ref. [9] that Weyl fermions were protected against scattering on phonons, through an analysis of the

temperature dependence of the scattering time. We also showed in Ref. [9] that they were protected against defect scattering, by comparing the effect on samples with mobilities differing by 2 orders of magnitude. We show here that they are not necessarily protected against scattering on charged particles like ionized impurities and electrons in trivial pockets.

Figures 2(c) and 2(d) show the magnetothermal conductivity of undoped Bi-Sb samples from $x = 0$ to $x = 0.224$ at 75 K. We normalize it to the zero-field thermal-conductivity value (shown in Fig. S3 within the Supplemental Material [24]) for comparison. The zero-field thermal conductivity decreases with increasing x because of phonon-alloy scattering, which is well understood in binary alloys. An important observation is that the intensity of the thermal chiral anomaly significantly depends on x, even though the crystal quality is nearly identical from sample to sample. As described above, at $x < 0.04$, we do not observe any thermal chiral anomaly because these compositions do not form a Weyl phase. However, when $x > 0.04$, we observe the thermal chiral anomaly up to $x = 0.203$ and the intensity of the thermal chiral anomaly increases as x increases up to $x = 0.105$ [Fig. 2(c)] and decreases as x increases to $x = 0.224$ [Fig. 2(d)]. In Fig. 2(e), we show $d\kappa/dB$ at 3 T for all undoped samples in the bottom panel. The top panel of Fig. 2(e) shows the energies of relevant band edges in Bi$_{1-x}$Sb$_x$ as a function of x corresponding to the description given in Sec. I. We find that $d\kappa/dB$ is maximized in a small window of x when the CB and VB are separated by a direct gap in the TI state. $d\kappa/dB$ is smaller when Bi$_{1-x}$Sb$_x$ has an indirect band gap, i.e., when trivial T- or H-hole pockets are thermally populated and provide a scattering channel between Weyl fermions and trivial holes, leading to a decrease in τ, as shown in Eq. (2). $d\kappa/dB$ tends to 0 at $x = 0.224$, similar to a trivial semimetal composition of $x = 0.02$, even though topological band inversion at the L point still exists at $x = 0.224$. From this first set of experiments, we conclude that, once trivial bands are within $k_B T$ of the chemical potential and populated, two things happen. First, they make the chemical potential shift away from the Weyl points, and second, electrons in trivial pockets may scatter Weyl fermions, indicating that these may not be protected against scattering on charged entities. To verify the first point, we present in the Supplemental Material [24] a simple estimate of how the chemical potential moves with increasing temperature in the bands of Bi$_{0.88}$Sab$_{0.12}$, a direct-gap semiconductor in its TI phase [24–27], and in Bi$_{0.82}$Sab$_{0.18}$, an indirect-gap semiconductor in its TI phase. The presence of a trivial band, particularly the H-hole band that is sixfold degenerate, and thus, has a very high density of states, shifts the chemical potential substantially away from the Weyl or Dirac points. In direct-gap semiconductors, the chemical potential falls in the midgap in the absence of unintentional doping (which is
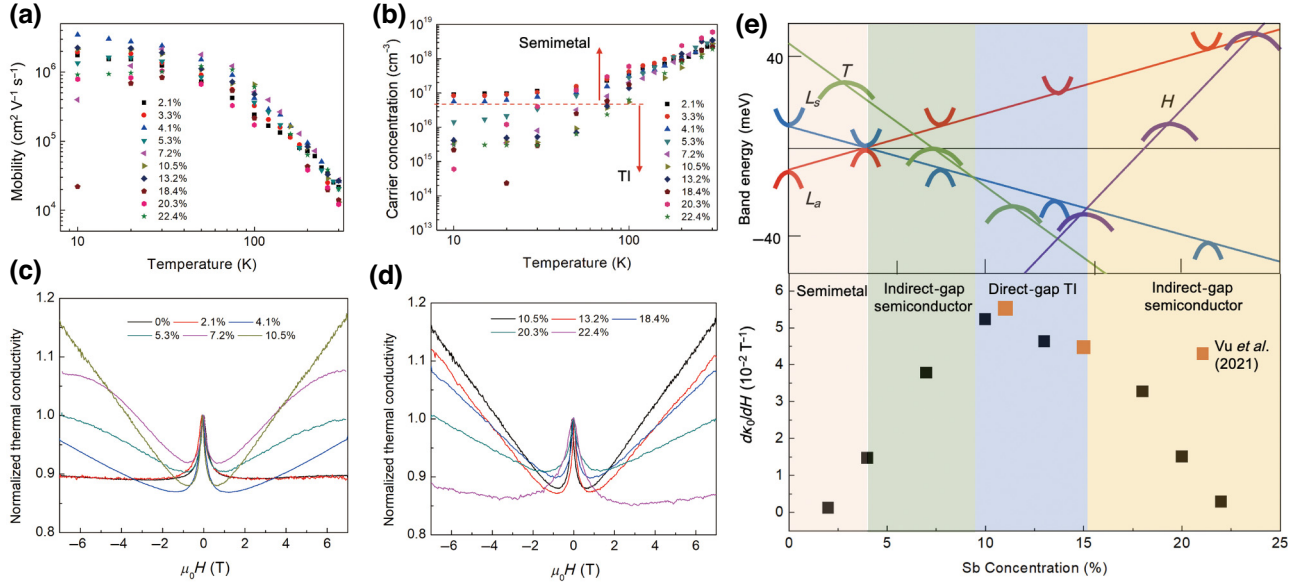
FIG. 2. Transport measurement of $Bi_{1-x}Sb_x$ crystals. (a) Temperature-dependent mobility of $Bi_{1-x}Sb_x$ alloys of the compositions shown in the figure. (b) Temperature-dependent carrier concentration of $Bi_{1-x}Sb_x$. Mobilities and carrier concentrations of samples with $x = 0.021$, $x = 0.033$, $x = 0.041$, $x = 0.053$, and $x = 0.072$ are obtained from the literature [10]. (c) Longitudinal magnetothermal conductivity along the (001) direction of $Bi_{1-x}Sb_x$ from $x = 0.021$ to $x = 0.105$, normalized to the zero-field value. (d) Longitudinal magnetothermal conductivity along (001) of $Bi_{1-x}Sb_x$ from $x = 0.105$ to $x = 0.224$, normalized to the zero-field value. (e) Top panel, evolution of the electronic band structure of $Bi_{1-x}Sb_x$ as a function of Sb concentration, from Refs. [9,16]. Bottom panel, Sb-concentration-dependent $d\kappa/dB$ at 3 T. $x = 0.11$ and 0.15 data are extracted from the literature [9].

minimal here) up to a temperature of 150–200 K. Above 200 K, the T and H-hole bands, though located deep in the valence band, become thermally populated, and the chemical potential shifts toward the conduction band to maintain charge neutrality in the crystal. Below that temperature, the samples are ideal Weyl semimetals, and no Shubnikov–de Haas oscillations are observed (see the Supplemental Material [24]) at 2 K. In indirect-gap semiconductors, such as $Bi_{0.82}Sb_{0.18}$, the chemical potential at a low temperature is pinned to the top of the H-point valence band, due to it high degeneracy and density of states. With increasing temperature, it shifts more rapidly toward the conduction band than in the case of $Bi_{0.88}Sb_{0.12}$. It is thus clear that this shift also contributes to the decrease in the intensity of the anomalous currents at $x > 13\%$.

Trivial pockets might act as a bath supporting chirality changes to Weyl fermions, thus allowing backscattering of topologically protected Weyl fermions. The thermal chiral anomaly is maximized when only inter-Weyl-point scattering is present and Weyl fermions from other charge-carrier scattering is negligible. Thus, band engineering to maximize the chiral anomaly in Weyl semimetals requires that the trivial bands be removed from the thermal energy range around the Weyl points.

Equation (2) predicts that the anomalous thermal conductivity increases linearly with temperature. However, we find that the chiral anomaly contributes less to thermal

transport at high temperature than predicted, even when inter-WP scattering is not so intense because scattering across the Weyl bands' bandwidth is not thermally activated. The discussion above suggests that this is a result of the temperature-induced change of the chemical potential *vis-à-vis* the Weyl points when trivial bands are populated. If this is true, shifting the chemical potential in direct-gap samples without trivial pockets present through doping should give an effect that is consistent with that of temperature. To provide further proof, we prepared a total of seven doped $Bi_{1-x}Sb_x$ samples at the concentration ($x \approx 0.1$) where the anomaly was maximum (see Table I). We choose $Bi_{0.9}Sb_{0.1}$ to study the effect of chemical potential because the Weyl band is the least influenced by trivial bands in this composition, and it shows the largest thermal chiral anomaly. In addition, since this composition has a direct gap at the L points, the chemical potential without doping is at the middle of the band gap at the L point in the TI phase, which corresponds to the WPs in the Weyl phase. It has little dependence on slight variations in x when we prepare different samples (this would not be the case for $x < 0.09$). To precisely control the chemical potential of $Bi_{0.9}Sb_{0.1}$, we use Sn as an acceptor and Te as a donor. Properties of the doped samples are summarized in Table I. S1–S3 are n-type doped and S4–S7 are p-type doped with different doping concentrations. Fig. S4(a) within the Supplemental Material [24]

shows schematics of expected chemical potential, μ_{S1}–μ_{S7}, in the limit for $T \to 0$ K, corresponding to samples S1–S7, respectively. The chemical potential is far away from the WPs when the carrier concentration (electron or hole) is high. Figures 3(a) and 3(b) show carrier mobilities and concentrations of the doped $Bi_{0.9}Sb_{0.1}$ samples. All the samples, except S3 and S7, show extremely high mobility near 1 000 000 $cm^2\,V^{-1}\,s^{-1}$ at 10 K, which is nearly identical to the quality of the undoped samples. For sample S7, we intentionally add large amounts of Sn above its maximum solubility in $Bi_{0.9}Sb_{0.1}$: the undissolved Sn is precipitated, producing intense defect scattering of the charge carriers and strongly reducing the mobility. This was done deliberately to illustrate the relationship between the thermal chiral anomaly and impurity scattering.

Figure 3(b) shows temperature-dependent carrier concentrations of doped $Bi_{0.9}Sb_{0.1}$. The temperature dependence of the carrier concentration is quite different, depending on whether the dopant is Te or Sn. The n-type samples behave like classical narrow-gap semiconductors; the electron concentration is saturated below a given temperature (T_{sat}) at a value that depends on donor concentration. The more the sample is doped, the higher the observed saturation temperature. At $T > T_{sat}$, the electron concentration increases due to the appearance of intrinsic thermally excited carriers. For n-type samples in the Weyl state (the Hall effect is measured in the TI state), the position of the chemical potential is the closest to WPs at and below T_{sat}. The Sn-doped samples behave quite differently, as previously studied [28]. The Sn-doped samples are all n type above 200 K, even the ones doped at the solubility level of Sn in Bi. Their polarity changes to p type at some temperature ($T_{n\text{to}p}$) that depends on the doping level. For example, the majority carrier polarity of S4 and S7 changes from p to n type at $T_{n\text{to}p} = 40$ and 180 K, respectively, which means that their chemical potential shifts from near the valence-band edge to near the conduction-band edge. In the Weyl state, it crosses the WP energy at $T_{n\text{to}p}$ and is away from the WPs when temperature is higher or lower than the n-to-p transition temperature. This particular behavior of the Sn-acceptor impurity is analyzed in the literature [28] and attributed to the fact that the acceptor level of Sn seems to be linked to the chemical potential rather than to the edges of the bands at the L point. Consequently, one expects the Sn atoms to be ionized only for $T < T_{n\text{to}p}$.

We measured the magnetothermal conductivity of doped $Bi_{0.9}Sb_{0.1}$ samples from -7 to 7 T at temperatures up to 200 K. In samples where the thermal chiral anomaly is small or zero, such as the $x = 0\%$ sample (Bi) shown in Fig. S2 within the Supplemental Material [24], the application of a magnetic field, even in the longitudinal direction, creates a strong positive magnetoresistance that, according to the Wiedemann-Franz law, results in a decrease of the electronic thermal conductivity. Unlike the resistivity,
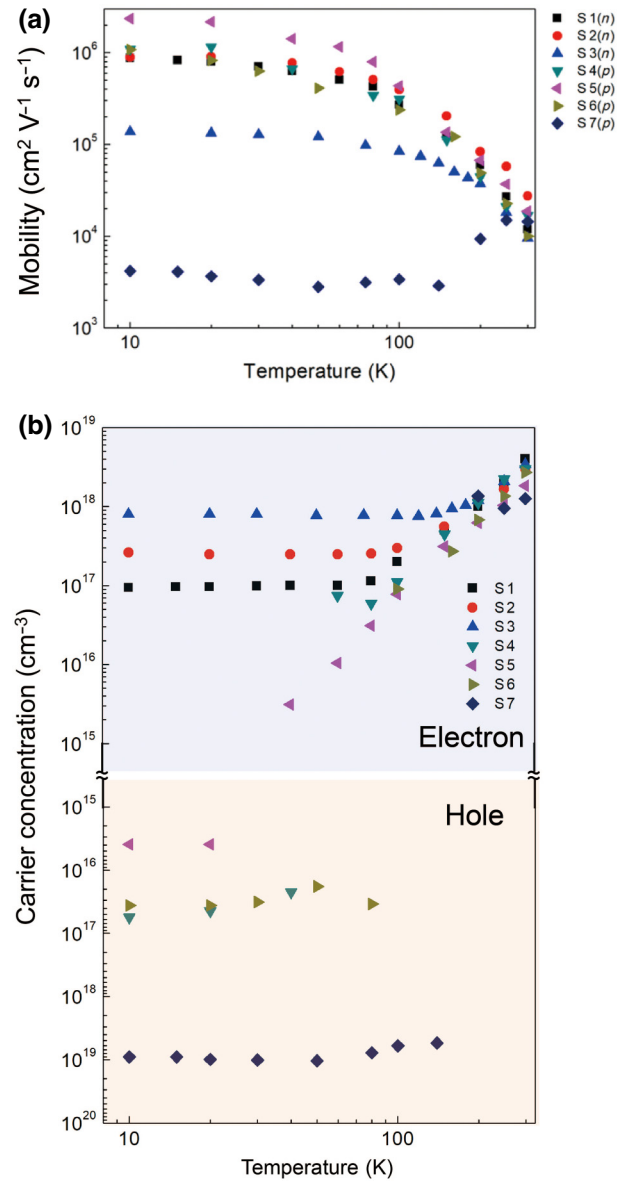

FIG. 3. Transport measurement of doped $Bi_{0.9}Sb_{0.1}$ samples. (a) Temperature-dependent carrier mobilities of the doped $Bi_{0.9}Sb_{0.1}$ samples. (b) Temperature-dependent carrier concentration of doped $Bi_{0.9}Sb_{0.1}$ samples. The p-type samples show a polarity change from n to p type at a characteristic temperature, $T_{n\text{to}p}$.

which increases monotonically, the thermal conductivity can only decrease until it reaches the value of the lattice thermal conductivity [29]. This technique is commonly used to separate electronic and lattice thermal conductivity in solids that have a large magnetoresistance and high mobility [30]. In $Bi_{0.9}Sb_{0.1}$, the anomalous thermal conductivity (κ_a) appears at high magnetic field after the sample has entered the Weyl phase, so that $\kappa = \kappa_p + \kappa_a$ is above the minimum in thermal conductivity observed at 1 T.
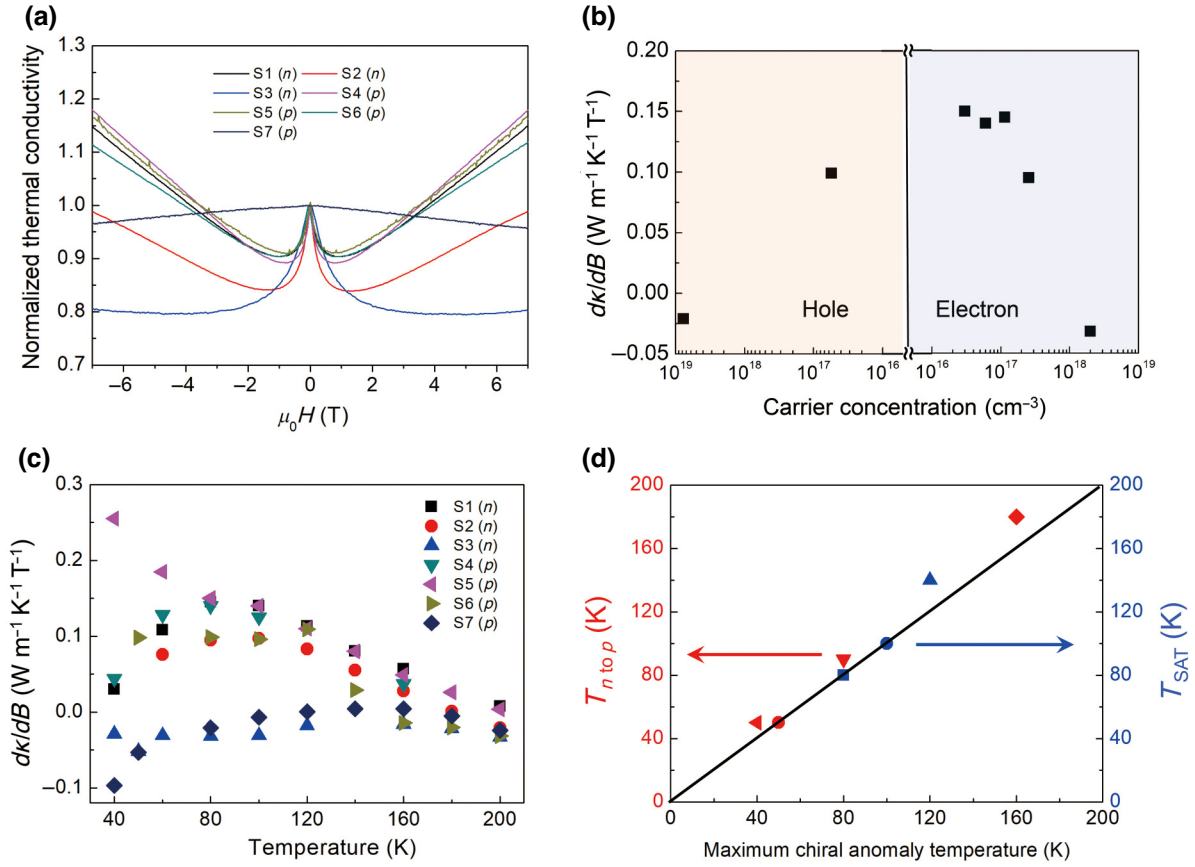
FIG. 4. Relationship between the anomalous thermal conductivity and chemical potential. (a) Longitudinal magnetothermal conductivity along the (001) direction of seven doped $Bi_{0.9}Sb_{0.1}$ samples, normalized to their zero-field values. (b) Field derivative, $d\kappa/dB$, at 3 T of the longitudinal magnetothermal conductivity along the (001) direction as a function of carrier concentration at 80 K. (c) Temperature dependence of $d\kappa/dB$ for seven doped $Bi_{0.9}Sb_{0.1}$ samples. (d) Relationship between the temperature at which the maximum anomalous conductivity is observed (abscissa) and the temperature, T_{sat}, at which the carrier concentration saturates in n-type samples (right ordinate) or the temperature, $T_{n to p}$, at which the n- to p-type transition is observed in the p-type samples.

In the next two paragraphs, we analyze the dependence of $d\kappa/dB$ on the doping levels [Figs. 4(a) and 4(b)] and the influence of charge neutrality on the maximum effect of the chiral anomaly [Figs. 4(c) and 4(d)].

Figure 4(a) summarizes the results for the seven doped $Bi_{0.9}Sb_{0.1}$ samples, normalized to the zero-field total thermal conductivity, at 80 K. The carrier concentrations of each sample S1–S7 at 80 K differ from those at 10 K (given in Table S1 within the Supplemental Material [24]) and are 9.42×10^{16}, 2.62×10^{17}, 8.01×10^{17}, 5.57×10^{16}, 3.90×10^{15}, 3.62×10^{16}, and 9.05×10^{18}, respectively. Sample S5 shows the largest anomalous conductivity at 80 K. The anomalous conductivity at 7 T is a 330% increase over κ_e and reaches 20% of κ_p. Figure 4(b) shows the carrier-concentration dependence of $d\kappa/dB$ at 80 K and 3 T. Here, high n-type or p-type carrier concentrations indicate that the chemical potential is located in the CBs or VBs and away from the Weyl points. Low carrier concentrations indicate that the chemical potential is near the middle of the band gap in the TI state, which

corresponds to the WPs in the Weyl state. Clearly, $d\kappa/dB$ decreases as the chemical potential is moved further from the charge-neutrality point, at a given temperature. Figure 4(b) demonstrates that the thermal chiral anomaly is maximized when the chemical potential is located at WPs at the temperature of the measurement.

The temperature dependence of the chemical potential in the doped samples also affects the magnitude of their anomalous conductivity. To verify that the temperature and doping-concentration dependence of the anomalous conductivity are consistent with one another, we plot $d\kappa/dB$ of all doped $Bi_{0.9}Sb_{0.1}$ samples as a function of temperature in Fig. 4(c). The temperature (T_{max}) at which the maximum chiral anomaly is observed varies with the doping concentration of the samples. The maximum anomalous $d\kappa/dB$ is observed at 80, 40, and 160 K for samples S4, S5, and S7, respectively. Comparing this to the temperature-dependent carrier concentration shown in Fig. 3(b), we find that the maximum chiral anomaly is observed at T_{sat} for n-type samples and at $T_{n to p}$ for p-type samples. Figure 4(d)

shows that the relationship between $T_{\max}$ and T_{sat} or $T_{n\text{to}p}$ and $T_{\max}$ falls nicely on a linear fit with both T_{sat} and $T_{n\text{to}p}$. This indicates that the thermal chiral anomaly is maximized when the chemical potential is at the middle of the band gap of the TI phase (the WPs in the Weyl phase). This conclusion is reached when this condition is reached either by varying the temperature or by varying the doping level.

To summarize, the Sb-concentration study and the doping-concentration study of the thermal chiral anomaly led to the same conclusions. It was shown in the literature [9] that thermal transport by Weyl fermions was protected from phonon and neutral defect scattering; in contrast, we show here that it is not protected from scattering on electrically charged particles. These can be trivial holes in the T or H bands of the indirect-gap TI state. The ionized impurities in the Te- and Sn-doped samples may play the same role. The Te donor is always ionized, and the anomaly decreases with increasing Te content. The Sn acceptor is ionized only at $T < T_{n\text{to}p}$ and, in particular, is charge neutral at $T_{n\text{to}p}$, where indeed the thermal chiral anomaly is maximum. Thus, to maximize the chiral anomaly and apply it to practical applications, the chemical potential and trivial electron (hole) bands need to be engineered. Once trivial bands are the least overlapped with Weyl bands and the chemical potential is on the WP, the thermal chiral anomaly is extremely high and contributes around 30% of the total heat current, and it is switchable by applying a magnetic field. We believe that our findings can significantly contribute not only to our fundamental understanding of Weyl fermions, but also to the application of WSMs to actively control heat flux.

All data are available in the main text or in the Supplemental Material [24].

ACKNOWLEDGMENT

Experiments were conducted by J.S.K., D.V., and M.Z. under supervision of J.P.H., who also conceived the study. All authors contributed to data analysis and writing of the manuscript.

The authors declare that they have no competing financial interests.

[1] C. L. Kane and E. J. Mele, Quantum Spin Hall Effect in Graphene, Phys. Rev. Lett. **95**, 1 (2005).

[2] D. Hsieh, D. Qian, L. Wray, Y. Xia, Y. S. Hor, R. J. Cava, and M. Z. Hasan, A topological Dirac insulator in a quantum spin Hall phase, Nature **452**, 970 (2008).

[3] M. Z. Hasan and C. L. Kane, Colloquium: Topological insulators, Rev. Mod. Phys. **82**, 3045 (2010).

[4] J. P. Heremans, R. J. Cava, and N. Samarth, Tetradymites as thermoelectrics and topological insulators, Nat. Rev. Mater. **2**, 1 (2017).

[5] S. Y. Xu, *et al.*, Discovery of a Weyl fermion semimetal and topological Fermi arcs, Science **349**, 613 (2015).

[6] G. Xu, H. Weng, Z. Wang, X. Dai, and Z. Fang, Chern Semimetal and the Quantized Anomalous Hall Effect in $HgCr_2Se_4$, Phys. Rev. Lett. **107**, 1 (2011).

[7] J. Gooth, A. C. Niemann, T. Meng, A. G. Grushin, K. Landsteiner, B. Gotsmann, F. Menges, M. Schmidt, C. Shekhar, V. Süß, R. Hühne, B. Rellinghaus, C. Felser, B. Yan, and K. Nielsch, Experimental signatures of the mixed axial-gravitational anomaly in the Weyl semimetal NbP, Nature **547**, 324 (2017).

[8] H. B. Nielsen and M. Ninomiya, The Adler-Bell-Jackiw anomaly and Weyl fermions in a crystal, Phys. Lett. B **130**, 389 (1983).

[9] D. Vu, W. Zhang, C. Şahin, M. E. Flatté, N. Trivedi, and J. P. Heremans, Thermal chiral anomaly in the magnetic-field-induced ideal Weyl phase of $Bi_{1-x}Sb_x$, Nat. Mater. **20**, 1525 (2021).

[10] J. S. Kang, D. Vu, and J. P. Heremans, Identifying the Dirac point composition in $Bi_{1-x}Sb_x$ alloys using the temperature dependence of quantum oscillations, J. Appl. Phys. **130**, 1 (2021).

[11] X. Huang, L. Zhao, Y. Long, P. Wang, D. Chen, Z. Yang, H. Liang, M. Xue, H. Weng, Z. Fang, X. Dai, and G. Chen, Observation of the Chiral-Anomaly-Induced Negative Magnetoresistance: In 3D Weyl Semimetal TaAs, Phys. Rev. X **5**, 1 (2015).

[12] Y. Wang, E. Liu, H. Liu, Y. Pan, L. Zhang, J. Zeng, Y. Fu, M. Wang, K. Xu, Z. Huang, Z. Wang, H. Z. Lu, D. Xing, B. Wang, X. Wan, and F. Miao, Gate-tunable negative longitudinal magnetoresistance in the predicted type-II Weyl semimetal WTe_2, Nat. Commun. **7**, 1 (2016).

[13] S. Liang, J. Lin, S. Kushwaha, J. Xing, N. Ni, R. J. Cava, and N. P. Ong, Experimental Tests of the Chiral Anomaly Magnetoresistance in the Dirac-Weyl Semimetals Na_3Bi and GdPtBi, Phys. Rev. X **8**, 1 (2018).

[14] N. P. Ong and S. Liang, Experimental signatures of the chiral anomaly in Dirac–Weyl semimetals, Nat. Rev. Phys. **3**, 394 (2021).

[15] R. G. Chambers, The conductivity of thin wires in a magnetic field, Proc. R. Soc. A **202**, 378 (1950).

[16] J. Heremans, C. M. Thrush, Y. M. Lin, S. B. Cronin, and M. S. Dresselhaus, Transport properties of antimony nanowires, Phys. Rev. B **63**, 854061 (2001).

[17] J. Heremans, C. M. Thrush, Y.-M. Lin, S. Cronin, Z. Zhang, M. S. Dresselhaus, and J. F. Mansfield, Bismuth nanowire arrays: Synthesis and galvanomagnetic properties, Phys. Rev. B **61**, 085406 (2000).

[18] D. R. Baker and J. P. Heremans, Linear geometrical magnetoresistance effect: Influence of geometry and material composition, Phys. Rev. B **13927**, 13927 (1999).

[19] G. Wehmeyer, T. Yabuki, C. Monachon, J. Wu, and C. Dames, Thermal diodes, regulators, and switches: Physical mechanisms and potential applications, Appl. Phys. Rev. **4**, 1 (2017).

[20] S. Cho, A. DiVenere, G. K. Wong, J. B. Ketterson, and J. R. Meyer, Transport properties of $Bi_{1-x}Sb_x$ alloy thin films grown on CdTe (111) *B*, Phys. Rev. B **59**, 10691 (1999).

[21] S. M. Koohpayeh, Single crystal growth by the traveling solvent technique: A review, Prog. Cryst. Growth Charact. Mater. **62**, 22 (2016).

[22] P. Cucka and C. S. Barrett, The crystal structure of Bi and of solid solutions of Pb, Sn, Sb and Te in Bi, Acta Crystallogr. **15**, 865 (1962).

[23] M. Shankar Narayana and N. Gopi Krishna, X-ray study of Bi, Sb and $Bi_{1-x}Sb_x$ alloys, Phys. Status Solidi A **202**, 2731 (2005).

[24] See the Supplemental Material at http://link.aps.org/supplemental/10.1103/PhysRevApplied.20.034014 for models used to calculate position of chemical potential. It also contains Refs. [25–27].

[25] J. Heremans and O. P. Hansen, Influence of non-parabolicity on intravalley electron-phonon scattering; The case of bismuth, J. Phys. C: Solid State Phys. **12**, 3483 (1979).

[26] M. P. Vecchi, E. Mendez, and M. S. Dresselhaus, in Proceedings of the 13th International Conference on Physics of Semiconductors (1976), pp. 459.

[27] J.-P. Issi, Low temperature transport properties of the group V semimetals, Aust. J. Phys. **32**, 585 (1979).

[28] J. Heremans and O. P. Hansen, Temperature dependence of excess carrier density and thermopower in tin-doped bismuth. Pseudo-parabolic model, J. Phys. C: Solid State Phys. **16**, 4623 (1983).

[29] V. D. Kagan and N. A. Red'ko, Phonon thermal conductivity of bismuth alloys, Sov. Phys. JETP **73**, 664 (1991).

[30] J. Heremans, M. Shayegan, M. S. Dresselhaus, and J. P. Issi, High-magnetic-field thermal-conductivity measurements in graphite intercalation compounds, Phys. Rev. B **26**, 3338 (1982).